Research Article | **Open Access**

Microstructures

Tao *et al.* *Microstructures* **2026**, *6*, 2026035 **DOI:**10.20517/microstructures.2025.124

Tailoring the optical transfer function of nonlocal metasurfaces for targeted image processing via an automated inverse design framework

Chengdong Tao[1], Chuanbao Liu[2], Yongliang Li[2], Siwen Qian[2], Wenmin Han[2], Feng Wang[1], Song Zhao[1], Feifei Ren[1], Yang Bai[2], Bo Li[1,3], Ji Zhou[1,4]

Keywords: Optical transfer function, automated inverse design, optical image processing, nonlocal metasurface

Citation: Tao, C.; Liu, C.; Li, Y.; Qian, S.; Han, W.; Wang, F.; Zhao, S.; Ren, F.; Bai, Y.; Li, B.; Zhou, J. Tailoring the optical transfer function of nonlocal metasurfaces for targeted image processing via an automated inverse design framework. *Microstructures* **2026**, *6*, 2026035. https://dx.doi.org/10.20517/microstructures.2025.124

Received: 26 Aug 2025 **First Decision:** 30 Sep 2025 **Revised:** 29 Oct 2025 **Accepted:** 21 Nov 2025 **Published:** 23 Mar 2026

Academic Editor: Yue Liu **Copy Editor:** Fangling Lan **Production Editor:** Fangling Lan

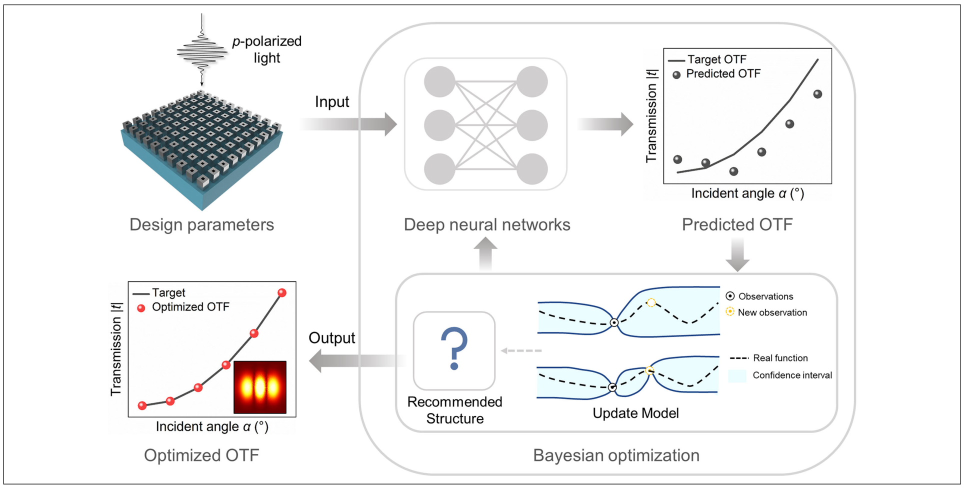

Abstract

Nonlocal metasurfaces exhibit significant potential for advanced all-optical image processing by leveraging their exceptional capability to regulate spatial dispersion through precise tailoring of optical transfer functions (OTFs). However, the inverse design of specific OTFs remains challenging due to the inherently complex and highly nonlinear relationship between metasurface structural parameters and angular-dependent optical responses, which conventional empirical trial-and-error approaches struggle to address. To overcome this limitation, we propose an automated inverse design framework integrating a deep neural network acting as a forward predictor with Bayesian optimization. This framework enables automated OTF tailoring by optimizing metasurface structural parameters for targeted image processing operations at desired wavelengths within the 1,200-1,400 nm range. We validate the framework by designing nine dedicated silicon hollow brick metasurfaces: for each operational wavelength (1,250, 1,300, and 1,350 nm),

---

[1]Suzhou Laboratory, Suzhou 215123, Jiangsu, China.
[2]Beijing Key Laboratory of Materials Intelligent Technology, Institute for Advanced Materials and Technology, University of Science and Technology Beijing, Beijing 100083, China.
[3]Tsinghua Shenzhen International Graduate School, Tsinghua University, Shenzhen 518055, Guangdong, China.
[4]State Key Laboratory of New Ceramics and Fine Processing, School of Materials Science and Engineering, Tsinghua University, Beijing 100084, China.

Correspondence to: Dr. Chengdong Tao, Suzhou Laboratory, Suzhou 215123, Jiangsu, China. E-mail: tcd0201@163.com; Prof. Yang Bai, Beijing Key Laboratory of Materials Intelligent Technology, Institute for Advanced Materials and Technology, University of Science and Technology Beijing, Beijing 100083, China. E-mail: baiy@mater.ustb.edu.cn; Prof. Bo Li, Suzhou Laboratory, Suzhou 215123, Jiangsu, China; Tsinghua Shenzhen International Graduate School, Tsinghua University, Shenzhen 518055, Guangdong, China. E-mail: boli@mail.tsinghua.edu.cn

three distinct devices are engineered to separately execute 2D second-order differentiation, 2D fourth-order differentiation, and 2D Gaussian high-pass filtering in transmission mode through targeted OTF engineering. These inversely designed nonlocal metasurfaces achieve a numerical aperture close to 0.4 and serve as fundamental components for edge detection and image sharpening. This intelligent, automated design paradigm dramatically accelerates the design process and significantly expands the scope of achievable functionalities for optical computing metasurfaces, paving the way for more sophisticated all-optical information processing systems.

INTRODUCTION

The relentless pursuit of faster, more efficient computation has increasingly shifted to photonic platforms[1-3]. Optical computing provides a compelling alternative to digital electronics by exploiting inherent advantages including massive parallelism, ultralow latency, and minimal energy dissipation. In particular, all-optical image processing, such as optical differentiation and spatial filtering, enables direct manipulation of optical wavefronts for critical tasks such as edge detection and image sharpening without optoelectronic conversion[4-7]. These capabilities form the critical foundation for emerging technologies spanning autonomous navigation, biomedical diagnostics, and augmented/virtual reality systems.

Traditionally, manipulating images in the spatial frequency domain relied on bulky 4f optical systems. Fourier optics principles dictate that such systems - employing paired lenses and a spatial filter - can perform optical image processing[8]. However, their inherent bulk impedes compact integration and miniaturization. The advent of metasurfaces, defined as subwavelength nanostructure arrays, has revolutionized nanophotonics and emerged as a transformative platform for image processing[9,10]. One class of metasurfaces is “local” metasurfaces, which modulate the optical wavefront by spatially varying the geometry or composition of individual meta-atoms across the surface. Implementing these as direct spatial filters in a 4f system remains bulky due to the long 4f distance and will be limited by paraxial approximation[11]. In contrast, nonlocal metasurfaces exploit collective resonances arising from interactions between identical meta-atoms[12-16]. This results in a spatially invariant response that directly modulates the Fourier components (angular spectrum) of the incident light. This unique property enables direct optical transfer function (OTF) engineering, allowing nonlocal metasurfaces to be seamlessly integrated as compact, lightweight elements at the input or output planes of various optical systems. Furthermore, their geometric uniformity makes them inherently compatible with scalable, high-throughput fabrication techniques (e.g., interference lithography and nanoimprint lithography), offering a significant practical advantage.

These compelling benefits - compactness, direct Fourier space manipulation, and fabrication scalability - position nonlocal metasurfaces as a transformative platform for real-time, all-optical image processing[17-20]. A wide variety of metastructures have been designed to perform optical analog computation[6,21]. However, a fundamental challenge impedes their widespread adoption: the complex, high-dimensional, and highly nonlinear relationship between the metasurface structure (e.g., unit cell geometry, periodicity, material) and its resulting angular optical response (the OTF). The design process has predominantly relied on manual, intuition-driven approaches, which are inherently limited in achieving on-demand inverse design for specific image processing tasks. This conventional paradigm is often inefficient and struggles to navigate the complex, highly nonlinear design space of nonlocal metasurfaces.

Recently, the introduction of deep neural networks (DNNs) has led to a significant change in the research paradigm of metasurfaces, greatly enhancing the design efficiency and diversity of metasurfaces[22-25]. In contrast to the conventional empirical trial-and-error approaches, the DNN learns the complex, nonlinear mappings between the structural parameters and optical responses, enabling highly accurate prediction of the optical responses and inverse design of desired metasurfaces. For example, Li *et al*. proposed physics-empowered forward and inverse DNN models to design dielectric meta-atoms with controllable multipole responses, avoiding time-consuming numerical simulations[26]. Chi *et al*. created a neural network-assisted end-to-end framework for gradient-based global optimization of multifunctional meta-optics, achieving full light-field control[27]. This approach outperforms fragmented design strategies by efficiently utilizing constrained parameter spaces for multi-wavelength-polarization holography. DNNs provide a powerful tool for efficiently designing metasurfaces with diverse functionalities. Moreover, integrating DNNs with intelligent optimization algorithms such as Bayesian optimization (BO) provides a framework for systematically navigating high-dimensional, non-convex design spaces using probabilistic surrogate models, efficiently finding global optima[28]. The synergistic integration of these techniques has already yielded breakthroughs in designing metasurfaces for perfect optical chirality. The self-consistent framework[28] that combines BO with convolutional neural networks to optimize optical properties of metallic nanostructures, establishing an efficient platform for property calculation and manipulation.

Here, we establish an automated inverse design framework for tailoring the OTF of a nonlocal metasurface, which integrates a DNN with BO. The DNN is pretrained to provide highly accurate predictions of the angular transmission spectrum of the nonlocal metasurface, while BO intelligently navigates the optimization of metasurface structural parameters based on the DNN-calculated results. Through this framework, we efficiently inverse design 2D second-order optical differentiator, 2D fourth-order optical differentiator and 2D Gaussian high-pass filter at the desired wavelengths of 1,250, 1,300 and 1,350 nm, respectively. These nonlocal metasurfaces achieve a numerical aperture (NA) close to 0.4 and serve as fundamental components for edge detection and image sharpening. This automated, intelligent design paradigm dramatically enhances the efficiency of designing optical computing metasurfaces, transcends the limitations of conventional approaches, and significantly expands the scope of achievable, complex optical functionalities. It paves the way for the realization of highly sophisticated, compact, and efficient all-optical information processing systems directly at the wavefront.

MATERIALS AND METHODS

Numerical simulations of the nonlocal metasurface

Numerical simulations are performed using the finite element method (COMSOL Multiphysics, Stockholm, Sweden) to calculate the angular transmission coefficients of the nonkocal metasurface[29]. The periodic systems are modelled using unit cells with periodic boundary conditions. The silica substrate and silicon material are set to be lossless dielectric layers, with refractive indices of 1.45 and 3.48, respectively. Moreover, it should be noted that all figures in this manuscript were generated based on simulation data from COMSOL Multiphysics and computational data from our inverse design model processed in Spyder (Python).

Automated inverse design framework

An automated inverse design framework integrating a DNN with BO is proposed for the optimization of a targeted nonlocal metasurface. The DNN, consisting of fully connected layers, is pretrained with the numerical data obtained from COMSOL to predict the OTFs of a nonlocal metasurface. Based on the calculated results of DNN, BO navigates the structural parameter space to achieve target OTFs at desired wavelengths.

RESULTS AND DISCUSSION

Description of the automated inverse design framework

The automated inverse design framework for tailoring the OTF of nonlocal metasurfaces, integrating a DNN-based forward prediction model with BO, is illustrated in Figure 1. The DNN is pretrained to accurately predict the angular transmission spectrum of nonlocal metasurfaces [Figure 1A-C]. BO then

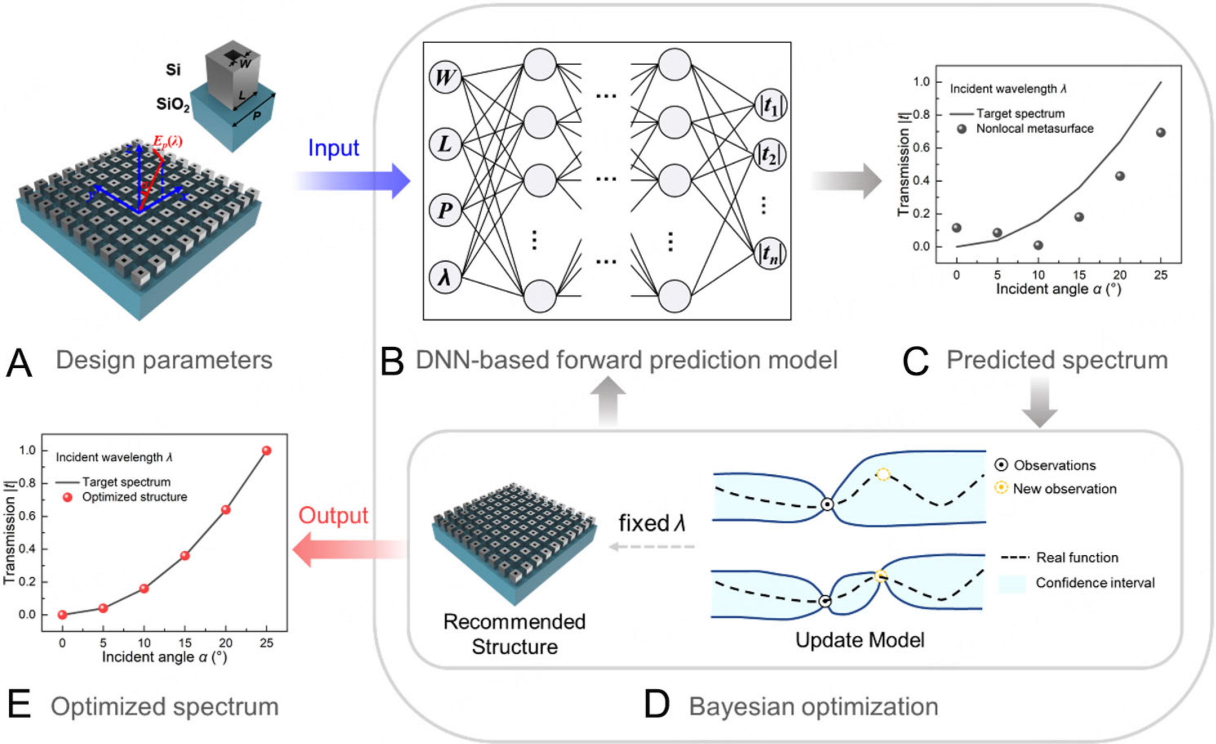

Figure 1. Schematics of the automated inverse design framework for tailoring the OTF of nonlocal metasurface. (A) Design parameters of the nonlocal metasurface. (B) Schematics of the DNN-based forward prediction model. (C) Predicted angular transmission spectrum of the nonlocal metasurface via DNN. (D) Schematics of the BO method. Recommended structural parameters from BO at fixed λ. (E) Optimized angular transmission spectrum of the nonlocal metasurface via BO.

navigates the structural parameter space to achieve user-specified OTFs at target wavelengths based on the calculated results of DNN [Figure 1D and E]. The metasurface comprises a periodic array of silicon hollow bricks exhibiting C4 symmetry (four-fold rotation symmetry) on a silica substrate. Key geometric parameters of the metasurface include internal hole edge length W, brick edge length L, unit cell period P, and fixed brick height H = 450 nm. Angular transmission spectra $|t_{pp}(\alpha)|$ (simplified as $|t(\alpha)|$) are characterized under p-polarized illumination across 1,200-1,400 nm wavelengths and incident angles (α) of 0°-25°, where p on the first and second subscripts denotes the polarization of the incident and transmitted light, respectively. Crucially, the metasurface OTF is derived from its angular transmission spectrum $|t(\alpha)|$ (see details in Supplementary Note 1).

The DNN input vector $[W, L, P, \lambda]$ encompasses structural parameters and operating wavelength λ, while its output vector $[|t_1|, |t_2|, ..., |t_n|]$ (n, number of incident angles) provides transmission magnitudes at discrete incident angles. The four parameters selected for optimization - hole edge length (W), brick edge length (L), unit cell period (P), and wavelength (λ) - were chosen based on their critical roles: λ is fundamental for on-demand inverse design at specific target wavelengths, whereas W, L, and P are the key geometric dimensions that directly govern the meta-atoms' spectral response via Mie scattering theory, thereby determining the resulting OTF [Supplementary Figures 1 and 2]. Pretrained DNN enables rapid computation of angular transmission spectra for design parameter sets. The BO module evaluates parameter-spectrum pairs at fixed λ, iteratively recommending improved structural parameters to the DNN. Through successive optimization cycles, metasurface configurations satisfying target spectral responses are obtained. This framework establishes an on-demand design platform for image-processing metasurfaces.

DNN-based forward prediction model

The DNN-based forward prediction model employs a fully connected architecture comprising an input layer, four hidden layers, and an output layer (see details in Supplementary Note 2). It establishes a complex mapping relationship between nonlocal metasurface design parameters [W, L, P, λ] and angular transmission spectra [$|t_1|$, $|t_2|$, ..., $|t_n|$]. The training data of the DNN is calculated by the COMSOL Multiphysics software using the finite element method (see Materials and Methods). A dataset of 57,645 distinct combinations of design parameters and angular transmission spectra is utilized to train and validate the DNN. The selection scheme for design parameters is as follows: the internal hole edge length W is in the range of 120-160 nm with an interval of 10 nm, the brick edge length L is in the range of 340-400 nm with an interval of 1 nm, the unit cell period P is in the range of 560-640 nm with an interval of 10 nm, and the incident wavelength λ is in the range of 1,200-1,400 nm with an interval of 10 nm. Moreover, the transmission spectra under different incident angles (α is in the range of 0°-25° with an interval of 5°) corresponding to each design parameter combination are obtained by COMSOL. To better evaluate the training performance of the DNN, the ratio of the training set, validation set and test set is set to 6:2:2. The performance of DNN is trained by minimizing the mean square error (MSE) loss between the predicted spectrum and the simulated spectrum. As shown in Figure 2A, the training loss and validation loss decreased rapidly and maintained a good degree of overlap, eventually stabilizing at the order of magnitude of 10^{-6} after training 600 epochs. Besides, the test loss is also as low as 2.9×10^{-6}, indicating a good training process. Consider the loss distribution of the test data, as shown in Figure 2B, 96% of test samples achieve MSE loss $< 1 \times 10^{-5}$, with all samples maintaining MSE loss $< 4 \times 10^{-5}$ on the test dataset. As shown in Supplementary Figures 3 and 4, the MSE distributions across the test data for different incident angles and different wavelengths have also been analyzed, respectively. The uniform and low-magnitude error distribution across both the angular and spectral domains confirms that our model does not introduce significant biases at physically sensitive points. As shown in Figure 2C-F, the predicted angular spectra of four randomly selected design parameter combinations are consistent with the simulated results. Besides, for parameters near the boundary of the design space (e.g., W = 120 or 160 nm), the prediction accuracy of the DNN is consistent with that of middle-range parameters [Supplementary Figures 5 and 6]. To evaluate the generalization performance of the DNN model, we have systematically analyzed the prediction errors of the DNN model over an expanded parameter range (W: 107-174 nm, L: 320-420 nm, and P: 533-667 nm), which corresponds to approximately 166.7% of the original parameter space range. We analyzed the model's performance by fixing one parameter at a time and evaluating the MSE and mean absolute error (MAE) across the remaining two parameters. As shown in Figure 3A-C, the MSE remains below 0.01 across most of the extended parameter space (W-L parameter space with P = 600 nm, λ = 1,300 nm; L-P parameter space with W = 140 nm, λ = 1,300 nm; W-P parameter space with L = 370 nm, λ = 1,300 nm) with only a slight increase in regions far outside the original training bounds. Furthermore, the distribution of the MAE for the transmission coefficient is illustrated in Figure 3D-F. The solid black boxes indicate the original training range, while the dashed boxes represent the expanded test range. Notably, even within this significantly enlarged parameter space, the MAE remains below 0.1, demonstrating the model's robust generalization capability. These results quantitatively confirm that the DNN model maintains high predictive accuracy within a broad neighborhood around the training domain, providing clear and practical guidance for its reliable application in metasurface design.

Recommendation of the nonlocal metasurface via BO

BO is a global optimization method used for black-box function optimization, and it is particularly suitable for computing expensive objective functions. BO is based on Bayesian theorem, which models the objective function by constructing a surrogate model (such as Gaussian Process), and uses the acquisition function to guide sampling, thereby efficiently finding the global optimal solution. In this work, BO is employed to recommend optimized structural parameters at fixed operation wavelength λ based on the current state of DNN model. By using the desired transmission angle spectrum as the objective function, and based on

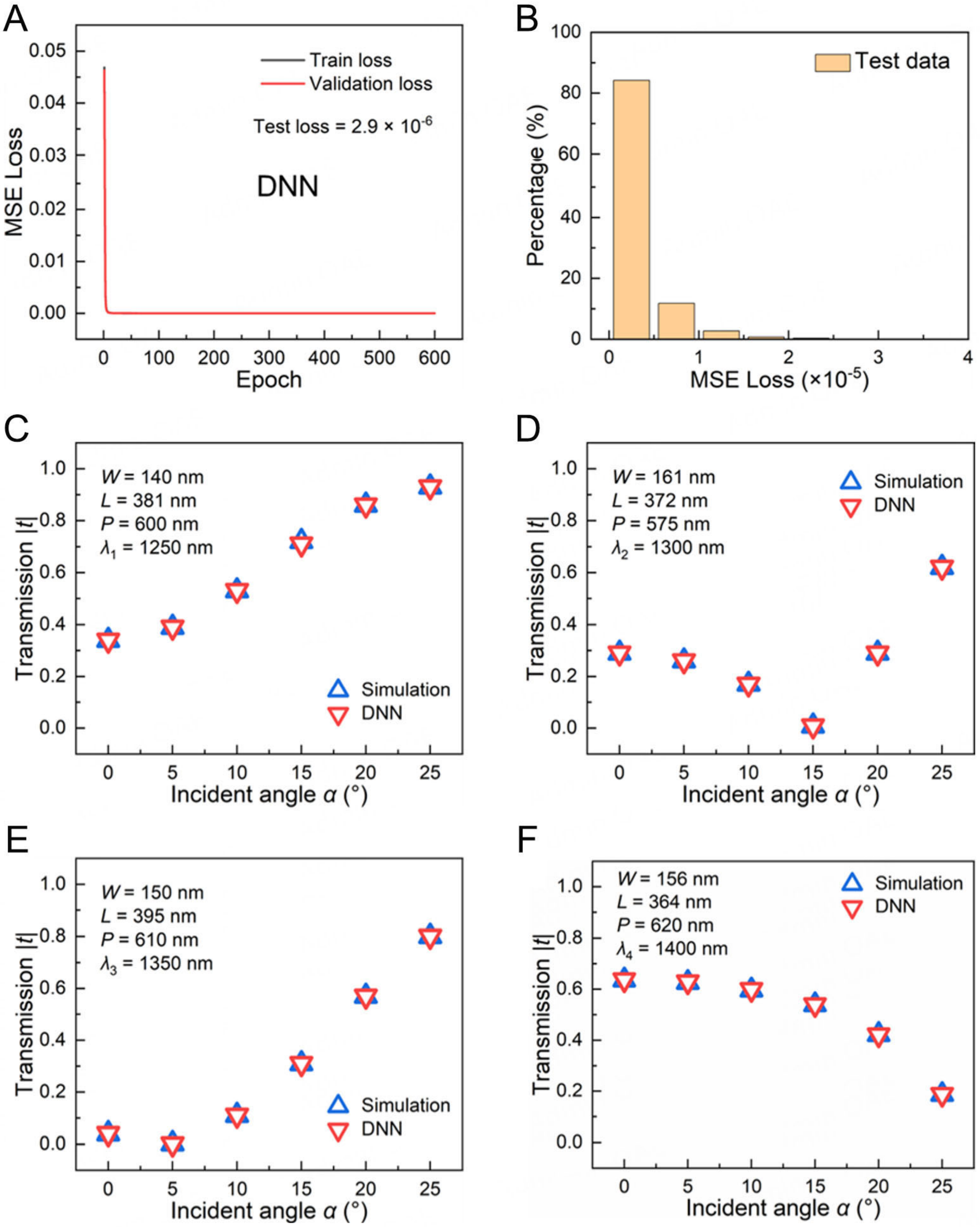

Figure 2. Forward prediction performance of the DNN. (A) Train loss, validation loss and test loss of the DNN. (B) Histogram of the MSE loss on test dataset for DNN. (C-F) Predicted performance of the DNN with four randomly selected design parameter combinations.

100 sets of data randomly predicted by the existing DNN model, BO continuously recommends new metasurface structures to minimize the difference between the angular transmission spectrum and the objective function. It then outputs the required metasurface structure. The BO integrated with a pretrained DNN will significantly accelerate the inverse design of a nonlocal metasurface. As summarized in Table 1,

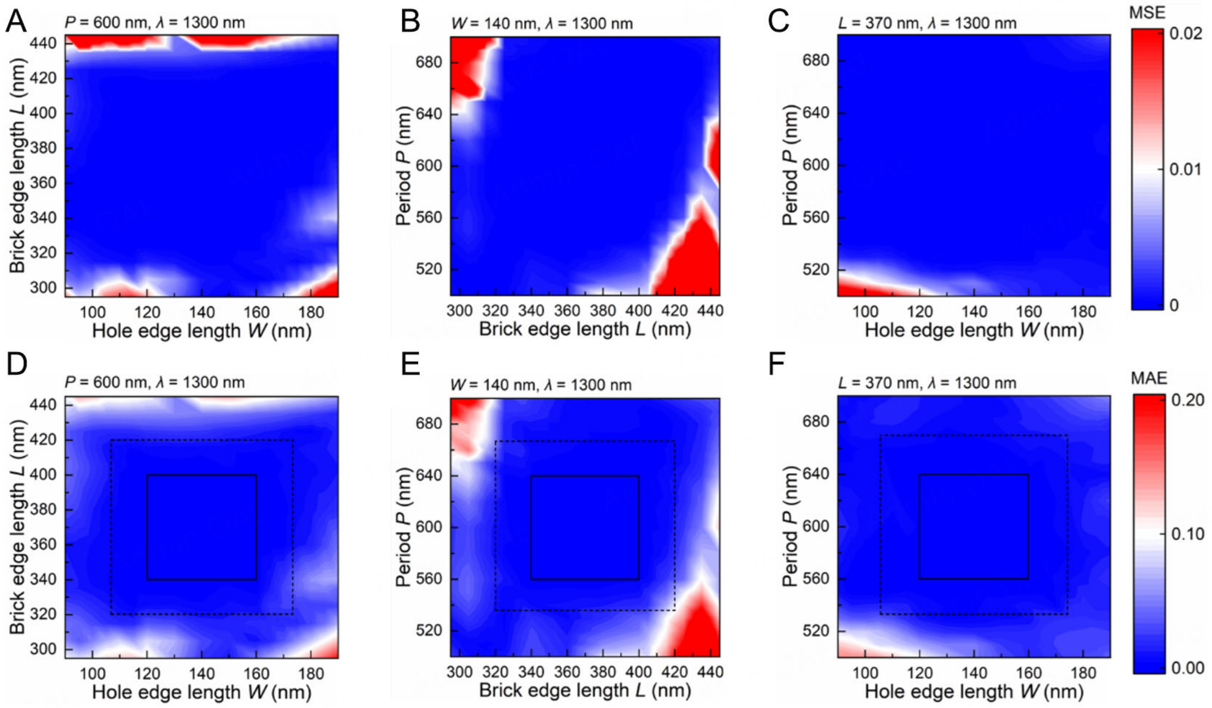

Figure 3. Evaluation of the DNN model's generalization performance. The MSE distribution of the DNN model within (A) the *W* and *L* parameter space, (B) the *L* and *P* parameter space and (C) the *W* and *P* parameter space, respectively. The MAE distribution of the DNN model within (D) the *W* and *L* parameter space, (E) the *L* and *P* parameter space and (F) the *W* and *P* parameter space, respectively.

Table 1. Quantitative comparison between the proposed automated inverse design framework and the traditional trial-and-error method

	With DNN + BO	With traditional trial-and-error method	Ratio
One-time forward prediction	0.03 s	24 s	800
Inverse design of metasurface	20 s	10,000 simulations (66.7 h)	12,000

DNNs: Deep neural networks; BO: bayesian optimization.

the BO-based optimization typically identifies a satisfactory solution within 100 iterations (≈20 s), whereas traditional brute-force numerical optimization or empirical trial-and-error methods require roughly 10,000 simulations, equivalent to about 66.7 h. This corresponds to a 12,000-fold acceleration in the inverse design process. It should be noted that this estimate is derived from the size of the parameter space under consideration. In designing image-processing metasurfaces at a target wavelength, we need to search over a multi-dimensional parameter space defined by structural variables such as width (*W*), length (*L*), and period (*P*). Due to the highly nonlinear mapping between the geometry and the angular spectrum response, the sampling intervals for these parameters must be sufficiently small. Assuming that each of the three parameters (*W*, *L*, *P*) is sampled with 100 possible values, the total number of simulations would be on the order of 10^6. Taking into account the potential for human-driven iterative improvement in empirical trial-and-error, we assume that roughly 1% of the full parameter space (i.e., ~10,000 simulations) would be explored before identifying a satisfactory solution. This estimation approach is consistent with that adopted in literature (see Supplementary Material in Ref.[30]).

Automated inverse design of optical differentiators

To demonstrate the automated inverse design performance of this framework, we carried out the inverse design of nonlocal metasurface-based optical differentiators with different orders at desired operation wavelengths, which are difficult for conventional empirical trial-and-error approaches. In the spatial frequency domain, the target angular transmission spectrum of the optical differentiator conforms to the following OTF $t(k_x,k_y)$:

$$t(k_x,k_y) = (ik_x)^m + (ik_y)^m \tag{1}$$

where k_x and k_y are wavevectors in the x and y directions, respectively, and m is the order of optical differentiator[7]. Owing to the C4 symmetry of the employed nonlocal metasurface, this framework can implement both 2D second-order and fourth-order optical differentiators. Without loss of generality, we consider an azimuthal angle of 0° under p-polarized incident light in transmission mode. The corresponding OTFs for these differentiators are given by:

$$t(k_x)_{\text{second-order}} \propto k_x^{\,2} \approx k^2 \cdot \alpha^2$$

$$t(k_x)_{\text{fourth-order}} \propto k_x^{\,4} \approx k^4 \cdot \alpha^4 \tag{2}$$

where k is the wavevector of incident light (see details in Supplementary Note 1)[14]. The transmission coefficient of second-order differentiator exhibits a quadratic relationship with the incident angle, while the fourth-order differentiator is related to the incident angle in a fourth-power relationship.

To demonstrate the working principle of the automated inverse design framework, we evaluate the optimization process of the second-order optical differentiator at the desired operation wavelength of 1,250 nm. According to Eq. (2), the target angular transmission spectrum of the second-order optical differentiator can be [0.00, 0.04, 0.16, 0.36, 0.64, 1.00]. Besides, the operation wavelength is fixed at 1,250 nm, the search ranges of W, L, and P are 120-160, 340-400, and 560-640 nm, respectively. We define the MSE between the inverse design angular transmission spectrum and the target angular transmission spectrum. BO optimizes and recommends new structural parameters W, L, and P by maximizing the value of -MSE, ultimately achieving the desired nonlocal metasurface. As shown in Figure 4, after using DNN to evaluate 100 sets of randomly generated structural parameter combinations, BO iteratively optimized 100 iterations and finally output the optimal structure. By separately examining the inverse design angular transmission spectra when iteration = 1, 38, and 80 (see insets in Figure 4), it can be observed that the angular transmission spectra of the designed nonlocal metasurface are increasingly closer to the target values, thereby verifying the effectiveness of the optimization process. It should be noted that there is a minimal difference among the inverse-designed nonlocal metasurfaces while changing the initial points during the optimization process, which confirms the robustness of our BO-based inverse design process in finding valid solutions regardless of the specific starting point [Supplementary Table 1].

By employing the automated inverse design framework, second-order and fourth-order optical differentiators at desired operation wavelengths of 1,250, 1,300 and 1,350 nm, respectively, are all accurately achieved [Figure 5], which exhibits an excellent inverse design capability (structural parameters of these nonlocal metasurface-based optical differentiators can be seen in Supplementary Table 2). Our automated inverse design framework enables rapid, on-demand design of multi-order optical differentiators at target wavelengths.

To verify the 2D isotropic angular response of these nonlocal metasurface-based optical differentiators under p-polarization, we analyze transmission coefficients for arbitrary wavevectors across azimuthal angles (φ) at

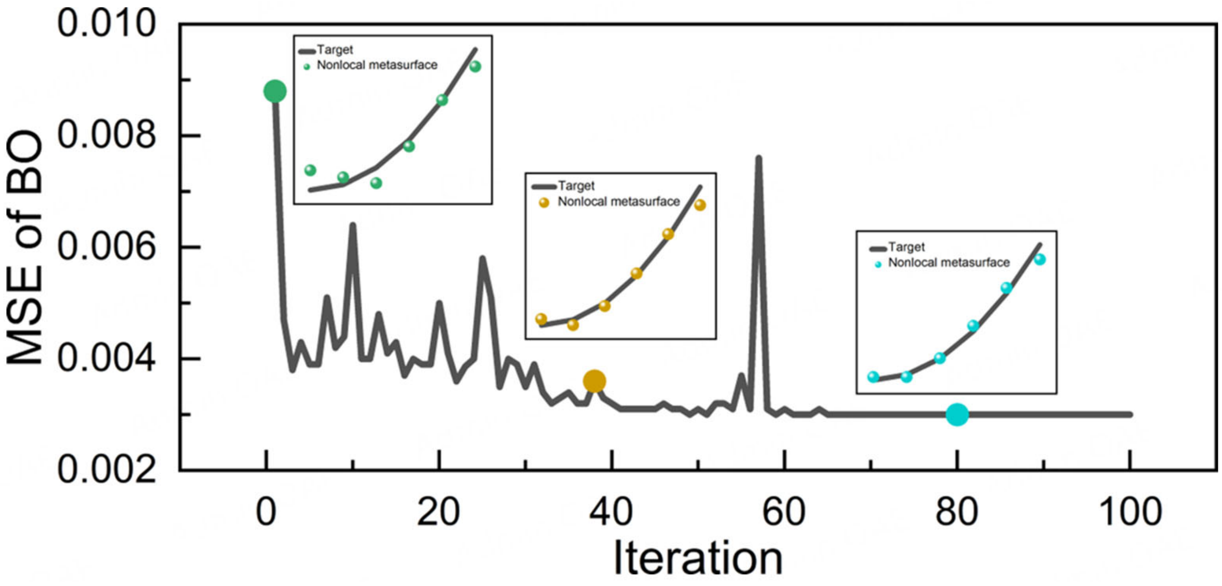

Figure 4. The optimization process of the BO-based framework. Inset: Angular transmission spectra of three intermediate structures during the optimization process.

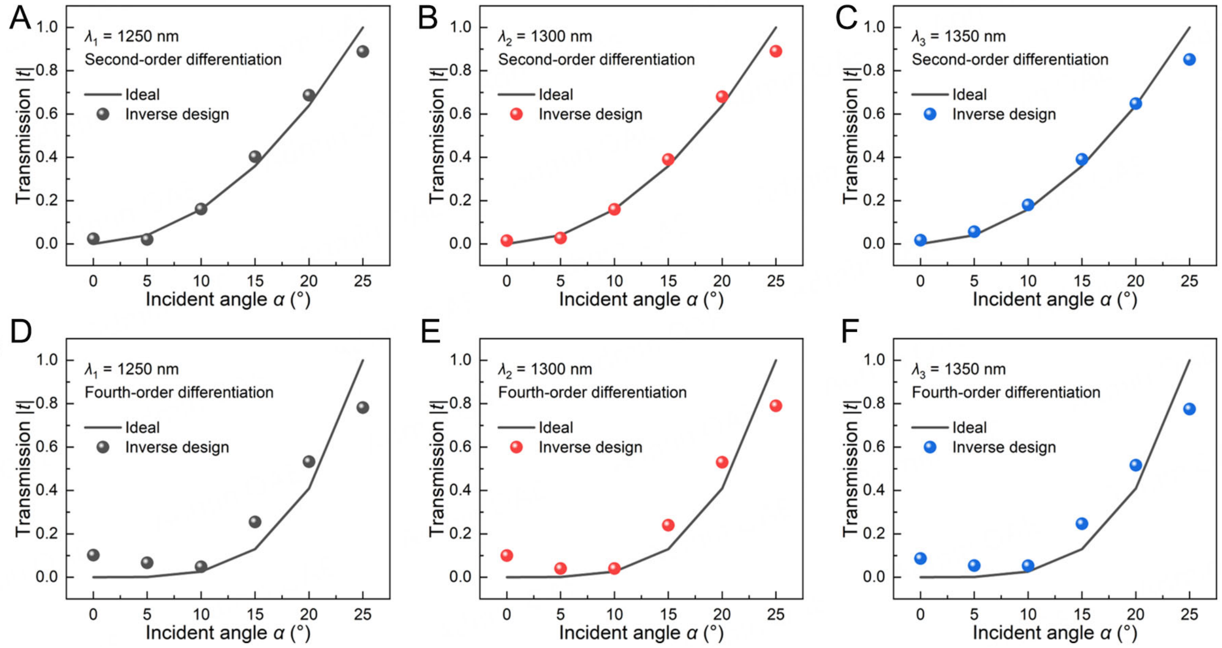

Figure 5. Automated inverse design of nonlocal metasurface-based optical differentiators. (A-C) Inverse design of second-order optical differentiators at desired operation wavelengths of 1,250, 1,300 and 1,350 nm, respectively. (D-F) Inverse design of fourth-order optical differentiators at desired operation wavelengths of 1,250, 1,300 and 1,350 nm, respectively.

1,250, 1,300 and 1,350 nm, respectively. Simulations sweep the in-plane incidence angle (α) from -25° to 25° in 5° increments, with φ ranging from 0° to 360° in 5° steps. As shown in Figure 6, the 2D transmission spectra of the second-order and fourth-order optical differentiators all exhibit near-circular profiles, which confirms consistent angular transmission behavior across azimuthal angles. Such azimuthal insensitivity under p-polarization ensures low-frequency wave components are suppressed while high-frequency components transmit uniformly across all directions within the ± 25° incidence range. Consequently, these results demonstrate that the silicon hollow brick metasurface functions as 2D isotropic second- and fourth-order optical differentiators under p-polarized light.

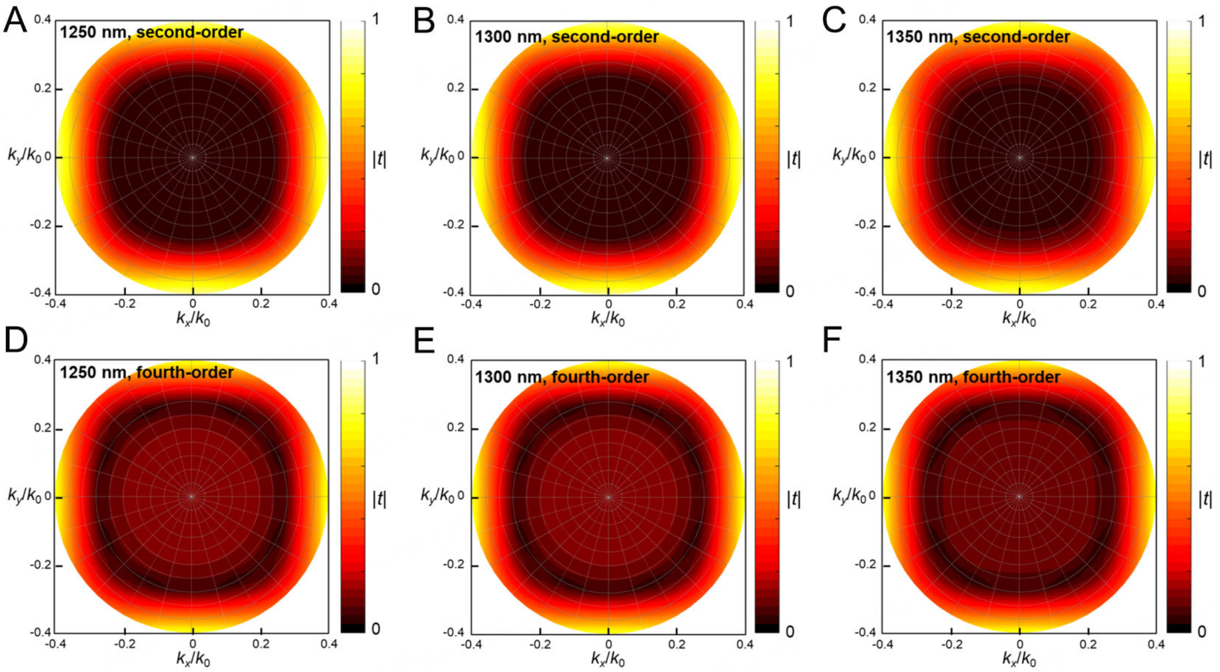

Figure 6. 2D isotropic angular responses of the nonlocal metasurface-based optical differentiators. (A-C) 2D transmission coefficients of second-order optical differentiators at desired operation wavelengths of 1,250, 1,300 and 1,350 nm, respectively. (D-F) 2D transmission coefficients of fourth-order optical differentiators at desired operation wavelengths of 1,250, 1,300 and 1,350 nm, respectively.

To further evaluate the optical differentiation performance of inverse-designed nonlocal metasurfaces, we simulated normally incident Gaussian beams on 20 × 20-pixel silicon hollow-brick metasurface arrays. Second-order differentiators transform the incident beam into a 1D horizontal lattice with three lobes in the normalized $|E_x|$ distribution [Figure 7A-C], while fourth-order differentiators generate five-lobe lattice patterns [Figure 7D-F]. These results align with theoretical predictions and experimental benchmarks[10], confirming successful implementation of second- and fourth-order differentiation. The inverse-designed metasurfaces thus function as effective analog optical differentiators.

We further analyzed the experimental feasibility of the inverse-designed nonlocal metasurface. According to existing literature[14], the fabrication process for silicon-based metasurfaces generally includes (1) depositing a silicon thin film of predetermined thickness on a silica substrate using pulsed laser deposition (PLD); (2) forming corresponding photoresist mask patterns via electron-beam lithography (EBL); and (3) etching the desired metasurface structures using inductively coupled plasma (ICP) etching. Throughout this process, the main sources of experimental deviation are the electromagnetic parameters (i.e., complex refractive index) of the silicon thin film and structural fabrication tolerances.

To address these two major sources of error, we evaluated their impact on the final experimental outcomes through both experimental and simulation-based approaches.

We prepared silicon thin films on silica substrates using PLD and measured their complex refractive index via spectroscopic ellipsometry. As shown in Figure 8, the measured imaginary part of the refractive index is close to 0, while the real part is approximately 3.48 within the 1,200-1,400 nm wavelength range - highly consistent with the values used in our simulations (3.48 + 0i). According to the specifications of the EBL

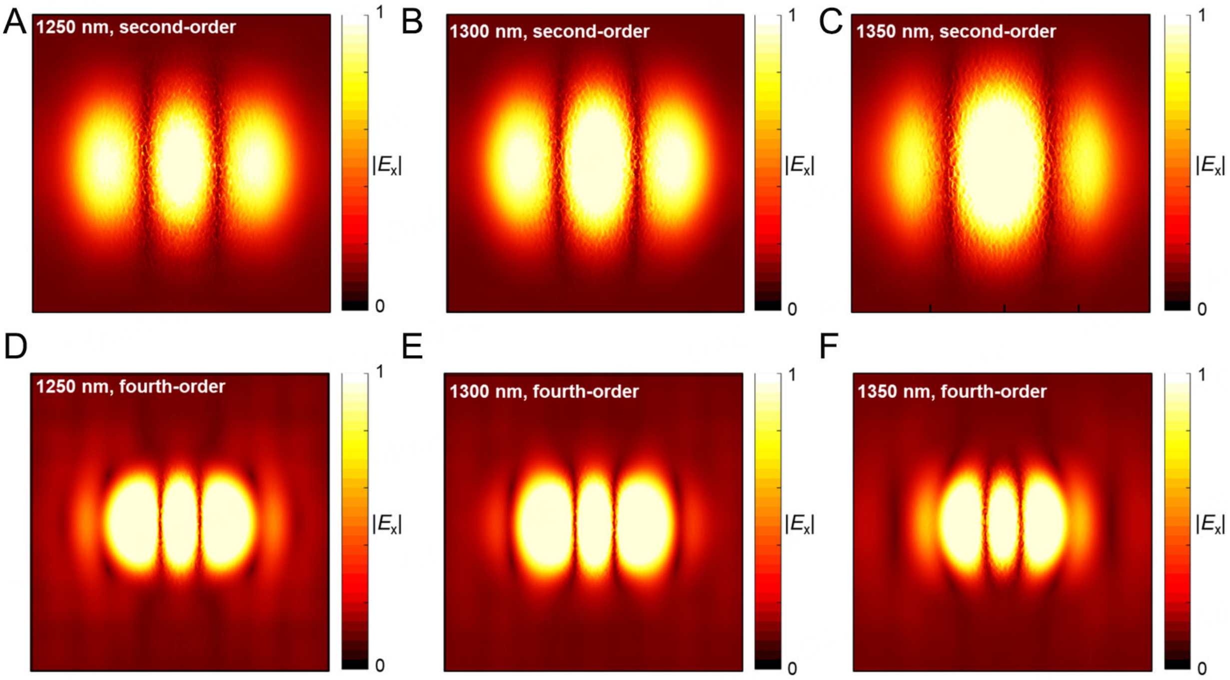

Figure 7. Nonlocal metasurface-based optical differential operations for Gaussian beam. (A-C) Normalized electric field |E_x| distributions of second-order optical differentiators under the normal incidence of Gaussian beam at 1,250, 1,300 and 1,350 nm, respectively. (D-F) Normalized electric field |E_x| distribution of fourth-order optical differentiators under the normal incidence of Gaussian beam at 1,250, 1,300 and 1,350 nm, respectively.

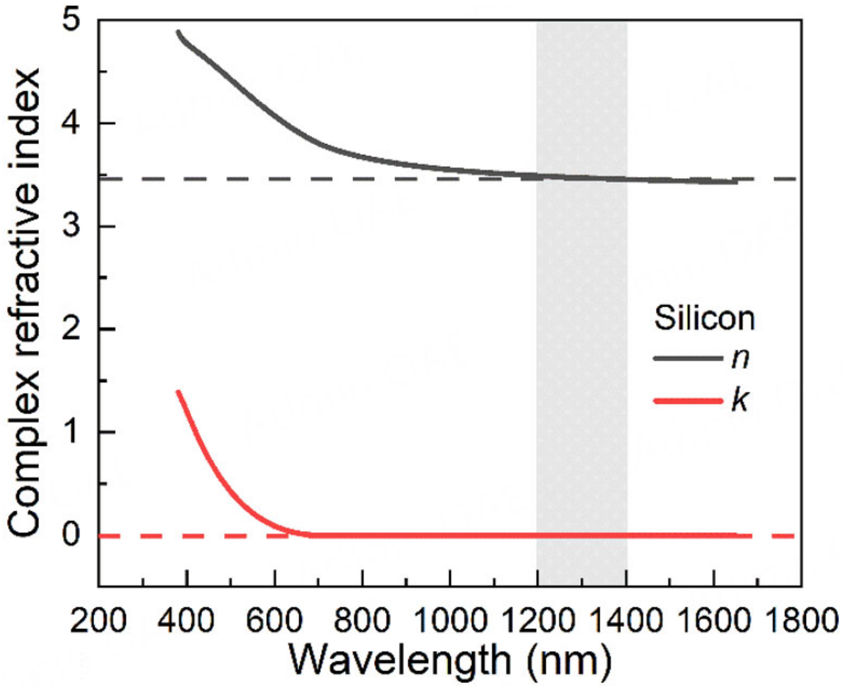

Figure 8. The complex refractive index of silicon film.

system (EBPG5200Plus) (see: https://raith.com/products/ebpg/), it supports high-resolution lithography down to below 5 nm. Assuming a 20% margin, the structural fabrication error is estimated to be within ± 1 nm. By comprehensively considering deviations in the complex refractive index and structural fabrication errors, we recalculated the optical transfer function of the second-order differential metasurface at 1,250 nm [Figure 9]. The results show good reproducibility compared to the originally designed optical response, supporting the reliability of our autonomous inverse design framework.

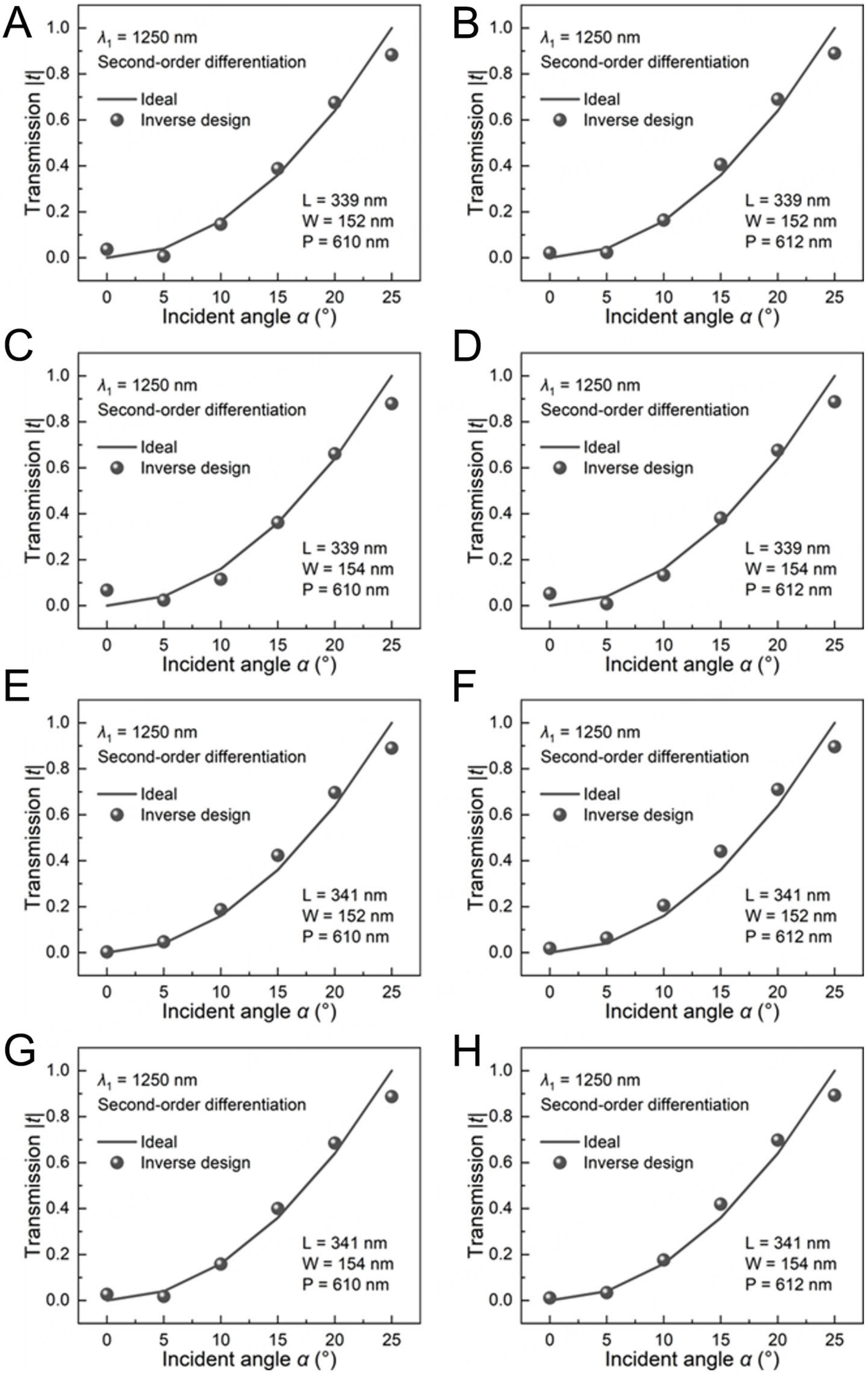

Figure 9. The OTFs of second-order differentiator at λ = 1250nm considering experimental deviations: (A) *L* = 339 nm, *W* = 152 nm, *P* = 610 nm; (B) *L* = 339 nm, *W* = 152 nm, *P* = 612 nm; (C) *L* = 339 nm, *W* = 154 nm, *P* = 610 nm; (D) *L* = 339 nm, *W* = 154 nm, *P* = 612 nm; (E) *L* = 341 nm, *W* = 152 nm, *P* = 610 nm; (F) *L* = 341 nm, *W* = 152 nm, *P* = 612 nm; (G) *L* = 341 nm, *W* = 154 nm, *P* = 610 nm; and (H) *L* = 341 nm, *W* = 154 nm, *P* = 612 nm.

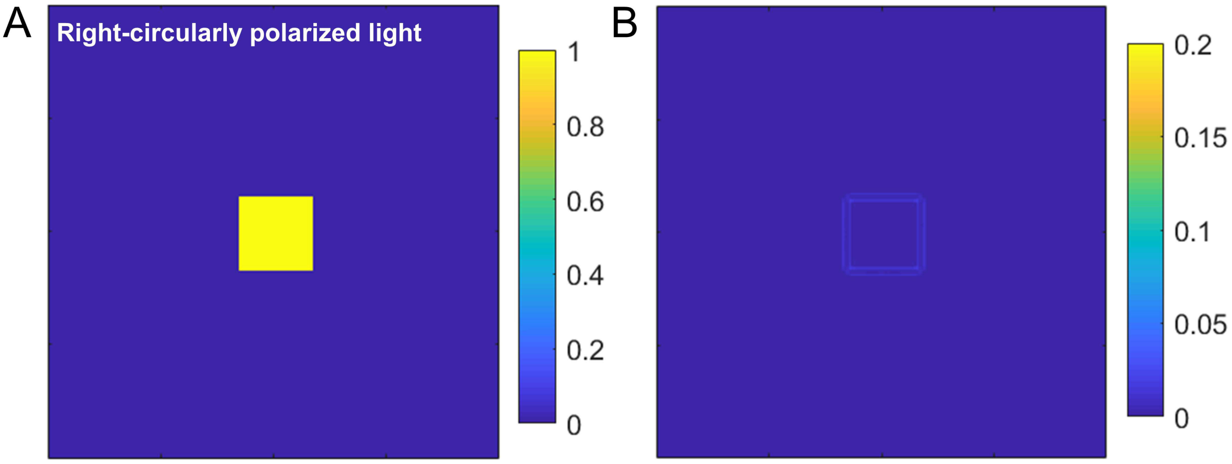

Figure 10. The theoretical image processing performance of the inverse designed second-order differentiator at λ = 1,250 nm, showing (A) the input test image (a yellow rectangle on a blue background) and (B) its theoretically processed output.

Moreover, we have performed additional simulations to quantitatively evaluate the image processing capabilities of our designed second-order differentiator metasurface (optimized for 1,250 nm). We simulated the processing of a standard test image (a yellow rectangle on a blue background, with a size of 200 μm × 200 μm, illuminated by circularly polarized light, as shown in Figure 10A) by our metasurface. The process involved: Applying a 2D Fourier transform to the input image, multiplying the result by the simulated 2D OTF of the metasurface, and performing an inverse Fourier transform to obtain the processed output image, which is the light intensity distribution. The result, shown in Figure 10B, clearly demonstrates successful edge detection, where the boundaries of the rectangle are significantly enhanced. To quantify this performance, we calculated the edge-to-noise ratio, which reached a value of 27. This high ratio indicates a sharp and clear edge detection effect with a good signal-to-noise level. The minimum feature size that the metasurface can effectively process is fundamentally determined by its NA and the operating wavelength. It can be estimated using the classic resolution formula $0.61 \cdot \lambda/\mathrm{NA}$[14]. For our design ($\lambda$ = 1,250 nm, NA = 0.4), this corresponds to a theoretical diffraction-limited feature size of approximately 1.9 μm.

Automated inverse design of Gaussian high-pass filters

To further investigate the performance of the automated inverse design framework, Gaussian high-pass filters in transmission mode at desired wavelengths have been achieved by tailoring the OTF of nonlocal metasurfaces. In the spatial frequency domain, the target angular transmission spectrum of the Gaussian high-pass filter conforms to the following OTF $t(u,v)$:

$$t(u,v) = 1 - e^{-D^2(u,v)/2D_0^2}, D(u,v) = \sqrt{u^2 + v^2} \tag{3}$$

$$u = k_x/2\pi, v = k_y/2\pi \tag{4}$$

where u, v are spatial frequency in the x and y directions, respectively, $D(u, v)$ is the distance from point (u, v) to the center of their spatial frequency, and D_0 determines the cutoff frequency of the filter[31]. Under the general assumption of an azimuthal angle of 0° with p-polarized light in transmission mode, the OTF for the Gaussian high-pass filter can be expressed by:

$$t(k_x) = 1 - e^{-k_x^2/8\pi^2 D_0^2} \approx 1 - e^{-k^2 \cdot \alpha^2/8\pi^2 D_0^2} \tag{5}$$

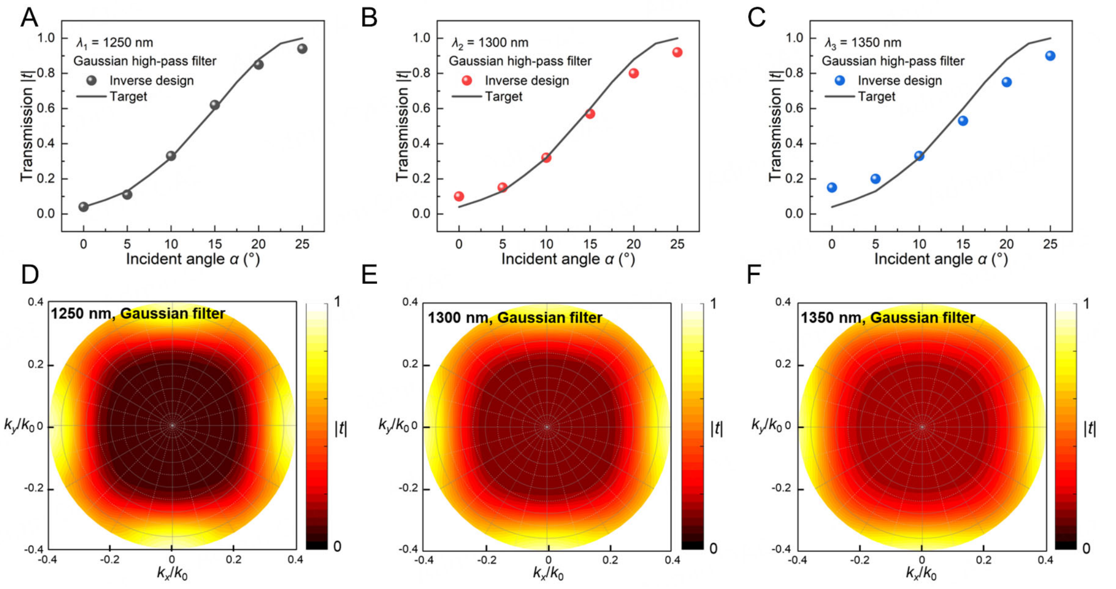

Figure 11. Automated inverse design of Gaussian high-pass filters. (A-C) Inverse design of nonlocal metasurface-based Gaussian high-pass filters at desired wavelengths of 1,250, 1,300 and 1,350 nm, respectively. (D-F) 2D isotropic angular responses of these Gaussian high-pass filters at desired wavelengths of 1,250, 1,300 and 1,350 nm, respectively.

(see details in Supplementary Note 1)[31]. As shown in Figure 11A-C, the target angular transmission spectra of the Gaussian high-pass filters can be obtained according to Eq. (5). Using the target OTF as the objective function for BO, we can efficiently inverse design and obtain the required nonlocal metasurfaces at three desired operation wavelengths 1,250, 1,300 and 1,350 nm, respectively. As shown in Figure 11A-C, the angular transmission spectra of the metasurface obtained through the automated inverse design framework closely match the target OTF (structural parameters of these nonlocal metasurface-based Gaussian high-pass filters can be seen in Supplementary Table 2), which demonstrates an efficient and accurate inverse-design performance. Moreover, due to the C4 symmetry of the silicon hollow bricks, these nonlocal metasurface-based Gaussian filters exhibit 2D isotropic angular response under different azimuthal angles [Figure 11D-F].

Comparisons between different AI strategies for metasurface inverse design

Numerous studies have explored AI-aided inverse design of metasurfaces in the current literature. To further demonstrate the efficiency of our automated inverse design framework, Table 2 provides a performance comparison between existing approaches and our DNN + BO method. Existing AI methods for metasurface design can be broadly classified into discriminative models, such as the Tandem DNN, and generative models, such as Generative Adversarial Networks (GANs) and Variational Auto-Encoders (VAEs)[32-35]. Although both types of models offer high optimization efficiency once trained, they are often susceptible to convergence at local optima, which can compromise design precision. In contrast, our DNN+BO framework maintains high optimization efficiency and achieves superior design accuracy compared to standalone neural network models. As summarized in Table 2, our approach employs a dataset of 57,645 samples, attains a prediction accuracy (MSE) below 4.0×10^{-5}, completes inverse design within 20 s, and achieves an average amplitude error (MAE) of 0.067 - highlighting a competitive balance among dataset scale, prediction accuracy, optimization speed, and design precision. The clear advantage of our proposed method stems from the integration of a well-trained forward neural network with BO. From a modeling perspective, the key benefits are as follows:

Table 2. Performance comparison between different AI strategies for metasurface inverse design

AI strategy	Dataset	Prediction accuracy (MSE)	Inverse design efficiency	Inverse design precision (MAE)	Reference
DNN + BO	57,645	$< 4.0 \times 10^{-5}$	< 20 s	average amplitude error = 0.067	This work
Tandem DNN	25,000	5.0×10^{-3}	0.05 s	frequency error < 2 nm	R[32]
GAN-based model	69,000	1.0×10^{-3}	0.3-36 s	amplitude error < 0.1	R[33]
VAE-based model	70,000	6.4×10^{-3}	0.01 s	phase error $< \pi/8$	R[34]
VAE-based model	51,000	8.2×10^{-2}	several mins	amplitude error < 0.1	R[35]

DNNs: Deep neural networks; BO: bayesian optimization; GAN: generative adversarial network; VAE: variational auto-encoder.

Table 3. Quantitative comparisons between the inverse designed nonlocal metasurfaces and other metasurface-based differentiators

Metasurface	Wavelength	Function	NA	Transmission efficiency	Reference
Silicon-based metasurface	Any wavelength within 1,200-1,400 nm	Second-order differentiator	0.4	0.77	This work
		Fourth-order differentiator	0.4	0.61	
		Gaussian high-pass filter	0.4	0.85	
Phase-change metasurface	1,050 nm	Second-order differentiator	0.5	0.81	R[12]
Silicon-based metasurface	1,155 nm	Second-order differentiator	0.4	0.76	R[14]
Silicon-based metasurface	Bandwidths of 35 nm around 1,500 nm	Second-order differentiator	0.35	0.81	R[19]
Silicon-based metasurface	1,560 nm	Second-order differentiator	0.35	0.81	R[36]

(1) The DNN is trained to learn the underlying physical laws governing the metasurface response - specifically, Maxwell's equations and Mie scattering theory. This enables the model to capture highly nonlinear physical interactions between structural parameters and optical responses, providing a more reliable and generalizable forward model compared to interpolation-based or linear methods.

(2) The DNN serves as a fast and accurate surrogate model, replacing computationally expensive numerical simulations. When combined with BO, which efficiently balances exploration and exploitation via an acquisition function, the method rapidly converges to high-performance designs. This avoids unnecessary simulations in suboptimal regions - a common drawback of brute-force and gradient-free optimization techniques. This combination allows us to locate near-optimal structural designs efficiently, without exhaustively simulating all possible configurations.

Compared to standalone approaches such as the Tandem DNN or generative models, our method achieves better design efficiency and higher accuracy by leveraging the neural network's fast inference and BO's sample-efficient global optimization. This modeling synergy substantially reduces the computational cost while maintaining high performance, offering a more scalable and systematic approach to metasurface design. Furthermore, compared with a manually designed nonlocal metasurface, this automated inverse design framework highlights a significant advancement in operational wavelength flexibility and function diversity [Table 3]. Besides, the second-order differentiator metasurface maintains its targeted functionality over a bandwidth of approximately 21 nm centered around the design wavelength of 1,250 nm [Supplementary Figure 7].

CONCLUSION

In conclusion, we have established an automated inverse design framework integrating DNN-based forward predictor with BO to tailor the OTF of nonlocal metasurfaces for targeted all-optical image processing. The DNN component serves as a high-accuracy forward model for angular transmission spectrum prediction, where 96% of test samples achieve MSE loss $< 1 \times 10^{-5}$, with all samples maintaining MSE loss $< 4 \times 10^{-5}$ on the test dataset. BO subsequently navigates the structural parameter space to achieve user-specified OTFs at desired wavelengths within the 1,200-1,400 nm range. Through this framework, we demonstrate precise OTF engineering on silicon hollow brick metasurfaces, realizing three key functionalities in transmission mode: 2D second-order differentiation, 2D fourth-order differentiation, and 2D Gaussian high-pass filtering at discrete operating wavelengths (1,250, 1,300, and 1,350 nm). These devices achieve NAs approaching 0.4 and enable effective edge detection and image sharpening. This paradigm shift from empirical design to intelligent automation dramatically accelerates metasurface development while expanding the functional horizon for optical computing applications.

DECLARATIONS

Authors' contributions

Conception and design of the study: Tao, C.; Liu, C.; Bai, Y.; Li, B.; Zhou, J.
Numerical simulation: Tao, C.; Li, Y.; Qian, S.
Automated inverse design framework: Tao, C.; Han, W.; Wang, F.; Zhao, S.; Ren, F.
Data analysis and interpretation: Tao, C.; Liu, C.; Bai, Y.; Li, B.; Zhou, J.
Writing: Tao, C.; Liu, C.; Bai, Y.; Li, B.; Zhou, J.
All authors have reviewed and edited the manuscript and agreed to the submission.

Availability of data and materials

The original contributions presented in this study are included in the Supplementary Materials. Further inquiries can be directed to the corresponding authors.

AI and AI-assisted tools statement

Not applicable.

Financial support and sponsorship

This work was supported by the National Natural Science Foundation of China (No. 92463311), the Basic Research Program of Jiangsu (No. SBK2024100236), and the Jiangsu Funding Program for Excellent Postdoctoral Talent.

Conflicts of interest

All authors declared that there are no conflicts of interest.

Ethical approval and consent to participate

Not applicable.

Consent for publication

Not applicable.

Copyright

Supplementary Materials

Supplementary Materials

REFERENCES

1. Mcmahon, P. L. The physics of optical computing. *Nat. Rev. Phys.* **2023**, *5*, 717-34. DOI
2. Xu, Z.; Zhou, T.; Ma, M.; Deng, C.; Dai, Q.; Fang, L. Large-scale photonic chiplet Taichi empowers 160-TOPS/W artificial general intelligence. *Science* **2024**, *384*, 202-9. DOI

3. Hua, S.; Divita, E.; Yu, S.; et al. An integrated large-scale photonic accelerator with ultralow latency. *Nature* **2025**, *640*, 361-7. DOI PubMed PMC
4. Chamoli, S. K.; Jin, C.; Fan, Y.; et al. Nonlocal flat optics for size-selective image processing and denoising. *Nat. Commun.* **2025**, *16*, 4473. DOI PubMed PMC
5. Zhou, Y.; Zheng, H.; Kravchenko, I. I.; Valentine, J. Flat optics for image differentiation. *Nat. Photonics*. **2020**, *14*, 316-23. DOI
6. Zangeneh-nejad, F.; Sounas, D. L.; Alù, A.; Fleury, R. Analogue computing with metamaterials. *Nat. Rev. Mater.* **2020**, *6*, 207-25. DOI
7. Silva, A.; Monticone, F.; Castaldi, G.; Galdi, V.; Alù, A.; Engheta, N. Performing mathematical operations with metamaterials. *Science* **2014**, *343*, 160-3. DOI PubMed
8. Goodman, J. W. Introduction to fourier optics; Englewood: Roberts and Company publishers; 2005. Available from: https://books.google.com/books?hl=en&lr=&id=ow5xs_Rtt9AC&oi=fnd&pg=PR7&dq=Introduction+to+Fourier+optics&ots=G_m2BK4GMK&sig=bQx1xvmNt3X_O9oHZZiuL1SM5KI#v=onepage&q=Introduction%20to%20Fourier%20optics&f=false [Last accessed on 20 Mar 2026].
9. Dorrah, A. H.; Capasso, F. Tunable structured light with flat optics. *Science* **2022**, *376*, eabi6860. DOI PubMed
10. Qiu, X.; Zhang, J.; Fan, Y.; Zhou, J.; Chen, L.; Tsai, D. P. Metasurface enabled high-order differentiator. *Nat. Commun.* **2025**, *16*, 2437. DOI PubMed PMC
11. Tanriover, I.; Dereshgi, S. A.; Aydin, K. Metasurface enabled broadband all optical edge detection in visible frequencies. *Nat. Commun.* **2023**, *14*, 6484. DOI PubMed PMC
12. Yang, G.; Wang, M.; Lee, J. S.; et al. Nonlocal phase-change metaoptics for reconfigurable nonvolatile image processing. *Light. Sci. Appl.* **2025**, *14*, 182. DOI PubMed PMC
13. Chen, Y.; Fleury, R.; Seppecher, P.; Hu, G.; Wegener, M. Nonlocal metamaterials and metasurfaces. *Nat. Rev. Phys.* **2025**, *7*, 299-312. DOI
14. Zhou, C.; Chen, Y.; Li, Y.; et al. Laplace differentiator based on metasurface with toroidal dipole resonance. *Adv. Funct. Mater.* **2024**, *34*, 2313777. DOI
15. Shastri, K.; Monticone, F. Nonlocal flat optics. *Nat. Photonics*. **2022**, *17*, 36-47. DOI
16. Kwon, H.; Sounas, D.; Cordaro, A.; Polman, A.; Alù, A. Nonlocal metasurfaces for optical signal processing. *Phys. Rev. Lett.* **2018**, *121*, 173004. DOI PubMed
17. Kwon, H.; Cordaro, A.; Sounas, D.; Polman, A.; Alù, A. Dual-polarization analog 2D image processing with nonlocal metasurfaces. *ACS. Photonics*. **2020**, *7*, 1799-805. DOI
18. Long, O. Y.; Guo, C.; Jin, W.; Fan, S. Polarization-independent isotropic nonlocal metasurfaces with wavelength-controlled functionality. *Phys. Rev. Appl.* **2022**, *17*, 024029. DOI
19. Cotrufo, M.; Arora, A.; Singh, S.; Alù, A. Dispersion engineered metasurfaces for broadband, high-NA, high-efficiency, dual-polarization analog image processing. *Nat. Commun.* **2023**, *14*, 7078. DOI PubMed PMC
20. Chen, A.; Monticone, F. Dielectric nonlocal metasurfaces for fully solid-state ultrathin optical systems. *ACS. Photonics*. **2021**, *8*, 1439-47. DOI
21. Abdollahramezani, S.; Hemmatyar, O.; Adibi, A. Meta-optics for spatial optical analog computing. *Nanophotonics* **2020**, *9*, 4075-95. DOI
22. Qian, C.; Kaminer, I.; Chen, H. A guidance to intelligent metamaterials and metamaterials intelligence. *Nat. Commun.* **2025**, *16*, 1154. DOI PubMed PMC
23. Chen, M. K.; Liu, X.; Sun, Y.; Tsai, D. P. Artificial intelligence in meta-optics. *Chem. Rev.* **2022**, *122*, 15356-413. DOI PubMed PMC
24. Li, Z.; Pestourie, R.; Lin, Z.; Johnson, S. G.; Capasso, F. Empowering metasurfaces with inverse design: principles and applications. *ACS. Photonics*. **2022**, *9*, 2178-92. DOI
25. Jiang, J.; Chen, M.; Fan, J. A. Deep neural networks for the evaluation and design of photonic devices. *Nat. Rev. Mater.* **2020**, *6*, 679-700. DOI
26. Li, W.; Barati, Sedeh. H.; Tsvetkov, D.; et al. Machine learning for engineering meta-atoms with tailored multipolar resonances. *Laser. Photonics. Rev.* **2024**, *18*, 2300855. DOI
27. Chi, H.; Hu, Y.; Ou, X.; et al. Neural network-assisted end-to-end design for full light field control of meta-optics. *Adv. Mater.* **2025**, *37*, e2419621. DOI
28. Li, Y.; Xu, Y.; Jiang, M.; et al. Self-learning perfect optical chirality via a deep neural network. *Phys. Rev. Lett.* **2019**, *123*, 213902. DOI
29. Tao, C.; Liu, C.; Li, Y.; Qiao, L.; Zhou, J.; Bai, Y. Efficient excitation of acoustic graphene plasmons for sub-nanoscale infrared sensing. *J. Opt. Soc. Am. B.* **2024**, *41*, 2280. DOI
30. An, S.; Fowler, C.; Zheng, B.; et al. A deep learning approach for objective-driven all-dielectric metasurface design. *ACS. Photonics*. **2019**, *6*, 3196-207. DOI
31. Makandar, A.; Halalli, B. Image enhancement techniques using highpass and lowpass filters. *Int. J. Comput. Appl.* **2015**, *109*, 21-7. DOI

32. Xu, L.; Rahmani, M.; Ma, Y.; et al. Enhanced light-matter interactions in dielectric nanostructures via machine-learning approach. *Adv. Photon.* **2020**, *2*, 1. DOI
33. An, S.; Zheng, B.; Tang, H.; et al. Multifunctional metasurface design with a generative adversarial network. *Adv. Opt. Mater.* **2021**, *9*, 2001433. DOI
34. Ma, W.; Xu, Y.; Xiong, B.; et al. Pushing the limits of functionality-multiplexing capability in metasurface design based on statistical machine learning. *Adv. Mater.* **2022**, *34*, e2110022. DOI
35. Zhang, N.; Gao, F.; Wang, R.; et al. Deep-learning empowered customized chiral metasurface for calibration-free biosensing. *Adv. Mater.* **2025**, *37*, e2411490. DOI
36. Cotrufo, M.; Singh, S.; Arora, A.; Majewski, A.; Alù, A. Polarization imaging and edge detection with image-processing metasurfaces. *Optica* **2023**, *10*, 1331. DOI